BISPECTRAL ANALYSIS OF ATTACHED EDDY MODELING OF WALL-BOUNDED TURBULENCE

Oles Dubrovski
Faculty of Mathematics
Technion Israel Institute of Technology
Haifa, 32000 Israel

Guangyao Cui
Faculty of Aerospace Engineering
Technion Israel Institute of Technology
Haifa, 32000 Israel

Ian Jacobi
Faculty of Aerospace Engineering
Technion Israel Institute of Technology
Haifa, 32000 Israel
ijacobi@technion.ac.il

ABSTRACT

Bispectral analysis was applied to the attached eddy model of wall-turbulence in order to examine whether the linear superposition of attached eddies can exhibit the spectral signature of non-linear, triadic scale interactions. Traditional analysis of scale interactions in turbulence has focused on correlations between filtered velocity signals of large- and small-scale motions. In contrast, the bispectrum provides a natural measure of non-linear scale interactions without filtering. The magnitude of the bispectrum represents the strength of the non-linear coupling, while the phase of the bispectrum represents a delay within the triadic interaction. In this study we utilized a numerical implementation of the attached eddy model to generate an ensemble of synthetic velocity fields, and we compared the averaged bispectrum of these fields to a DNS channel flow. The linear superposition of discrete hairpin packets was found to produce a similar bicoherence signature to that of velocity fields generated via true non-linear interactions, although the nature of the wavenumber coupling differed significantly. The biphase behavior of the attached eddy model also differed from the DNS. Tentative interpretations of both of these differences are offered in the context of the linear superposition mechanism, itself.

BACKGROUND

Scale-Interactions In Wall-bounded Turbulence

The interactions between large- and small-scale features of wall-bounded turbulence represent the primary mechanism for energy transfer in turbulence and thus a key target for developing turbulence models and efficient flow control strategies. Bandyopadhyay & Hussain (1984) first proposed a cross-correlation diagnostic to measure the relationship between the filtered large- and small-scale signals of a turbulent shear flow, and showed that the two scales are related in a way that varies across the width of the shear layer. This approach was later refined and extended by Mathis *et al.* (2009) and others who reported that large- and small-scale motions were positively correlated near the wall and inversely correlated near the free-stream of a turbulent boundary layer, in a pattern reminiscent of the streamwise skewness profile. The correlation between the different scales has been variously interpreted as the result of amplitude or frequency modulation of the envelope of small scale motions by large scales, or a spatial phase delay between the scales.

Duvvuri & McKeon (2015) performed a formal analysis of the scale correlation coefficient which showed that despite the somewhat artificial filtering of the velocity signal into large- and small-scale components, in reality the correlation coefficient represented interactions across three triadically-coupled scales. This observation is a direct consequence of the convective non-linearity of the incompressible Navier Stokes equations when written in spectral form, which allows only non-linear interactions between triadically coupled wavenumbers $\mathbf{k}'$, $\mathbf{k}''$, and $\mathbf{k} = \mathbf{k}' + \mathbf{k}''$. In light of this, Cui & Jacobi (2021) proposed that a non-linear diagnostic tool which accounts for the three distinct wavenumbers would be better suited to the scale-interaction analysis than the traditional two-component, cross-correlation.

Bispectral Analysis

The type of quadratic, non-linear interactions generated through turbulent convection are naturally described by the bispectrum, $B(k', k'')$, which is the third-order spectrum of a signal, $u(x)$, defined as:

$$B(k',k'') = \left\langle \widehat{u}(k')\widehat{u}(k'')\widehat{u}^*(k'+k'') \right\rangle . \qquad (1)$$

Just as the sum of the traditional, second-order power spectrum is related to the statistical variance, $\langle u^2 \rangle$, the bispectrum is related to the statistical skewness $\langle u^3 \rangle$ by $\langle u^3 \rangle = \sum_{k',k''} B(k',k'')$. However, unlike the real-valued power spectrum, the complex bispectrum preserves phase information between triadically interacting modes in addition to the amplitude information which describes the magnitude of the triadic coupling.

Recently, the bispectrum has received increased interest due to its preservation of triadic interaction information.

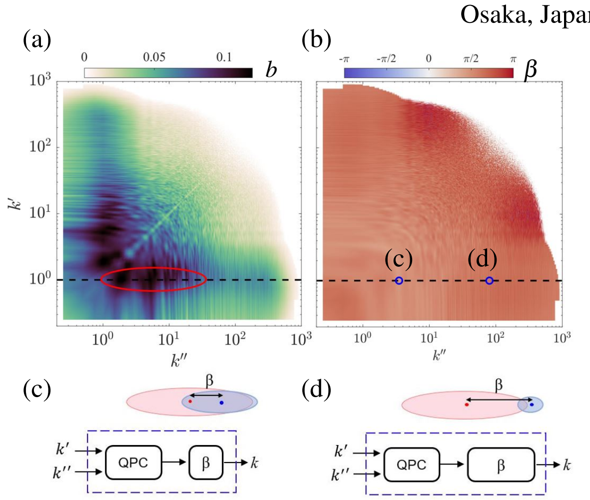

Figure 1: (a) The streamwise, normalized bispectrum (bicoherence), $b(k'',k')$, of a turbulent channel flow DNS evaluated at $y^+ \approx 281$. Note the high level of bicoherence associated with the LSMs circled in the red ellipse. (b) The corresponding biphase map, $\beta(k'',k')$, marked with two different phase locations corresponding to an interaction between (c) two LSMs and (d) an LSM with a smaller scale motion. The quadratic phase-coupled (QPC) interaction and phase delay for the two scales are illustrated schematically in panels (c) and (d) (corresponding to the circular marks), where the phase delay, β, is illustrated spatially but in reality represents a more complicated function of the interacting modes.

Dimension	Inner Units
Height	$H \approx 128$
Leg Gaussian Vorticity Std.	$\sigma = 0.05H \approx 6.4$
Leg Effective Radius	$R \approx 3\sigma \approx 19.2$
Streamwise Spacing	$b = 0.4H \approx 50$
Packet Length	$L_p = 6b \approx 300$
Vertex Angle between Legs	45°
Hairpin Inclination Angle	$\theta = 80^\circ$
Packet Inclination Angle	$\alpha = 10^\circ$
Number of Radial Fibers	$n_r = 20$
Numer of Azimuthal Fibers	$n_t = 40$
Distance Between Radial Fibers	$d_r = R/n_r \approx 0.96$
Azimuthal Distance Between Fibers	$R(2\pi/n_t) \approx 3$
Fiber Longitudinal Segment Length	≈ 5.7

Table 1: Top: The dimensions for the self-similar hairpin geometry corresponding to the smallest hairpin packet, defined by its height, H. Packets are sampled uniformly from the family of packets with heights $\{1,2,4,8,16\}H$, where all length dimensions in the table are scaled proportionally. Bottom: The dimensions of the discrete fibers used to represent the hairpin vorticity distribution for the Biot-Savart calculation.

Schmidt (2020) defined a bispectral modal decomposition for low-order representation of turbulent flows. Cui & Jacobi (2021) utilized the normalized amplitude (bicoherence, b) and phase (biphase, β) of the bispectrum to study the scale interactions in a turbulent channel flow and found that the dominant coupling between scales was associated with the large-scale motions (LSMs) of the channel flow interacting with a range of other scales, from other LSMs down to smaller scales, as shown in figure 1(a). They also showed that the biphase between the triadic interactions varied with scale size and could be interpreted as an interaction delay associated with the scale interactions, as illustrated in figure 1(b). However, the precise meaning of this interaction delay was not fully explored. In particular, does the biphase represent an interaction delay due to spatial proximity of the different scale velocity modes, or is it a result of temporal proximity due to variations in their respective convection velocities? And is the interaction delay associated with the particular geometry of the velocity mode shapes? These questions have important implications for modeling efforts involving the superposition of large-scale velocity modes to reconstruct turbulent flow fields. In order to address these questions, we apply the bispectral analysis to velocity fields constructed from a physically-meaningful model of large-scale motions – the attached eddy model, which involves only linear, spatial-superposition.

METHOD

Simulation via Attached Eddy Model

Townsend's attached eddy model presents a fundamentally physical approach to explaining the statistical properties of wall-bounded turbulence by constructing the turbulent velocity field via the superposition of hierarchies of self-similar eddies. Although first applied analytically to understanding the logarithmic mean velocity profile, it was later extended by Perry & Chong (1982) to describe higher order statistics as well, via spectral analysis. Perry (1987) also applied the attached eddy model numerically by assuming a particular form of the hairpin vortex, calculating the induced velocity field, and distributing these induced velocities randomly in space according to a reciprocal distribution with respect to eddy size. de Silva *et al.* (2016) and Eich *et al.* (2020) have since refined this numerical approach to better align the predicted velocity fields with experiments.

In the present study, we implemented a version of the numerical attached eddy model, following the hairpin packet specifications of de Silva *et al.* (2016). Each individual hairpin was composed of a bundle of discrete, parabolic vortex fibers, with a Gaussian vorticity distribution with standard deviation, σ across the bundle. The fiber bundles were arranged to construct the individual hairpins and then a packet of multiple hairpins with maximum height, $H = 128$ (inner units), as shown in figure 2. The geometric parameters describing the individual hairpins and the discrete fibers are detailed in table 1.

The Biot-Savart law was then applied to the vorticity field described by the fibers in order to generate the induced velocity field from the entire packet. Because the packets were geometrically self-similar, they could be scaled up in factors of 2^nH to obtain larger packets, where n represents the number of generations of hairpins. The maximum multiple considered here, $H_{\max} = 2^4H = 2048$ (limited by computer memory resources) represents the half-height of the simulated channel flow field and thus also corresponds to its friction Reynolds number, Re_τ.

The velocity fields of the hairpin packets were then uniformly, randomly selected from the geometric set of packet sizes, and the packet velocity fields were superposed in a uniform, random process to construct an individual volumetric flow snapshot of a channel flow. The channel domain extended 24 half-channel heights in the streamwise direction and 4 in the spanwise direction, with uniform spatial resolution, $\Delta x^+ \approx 20$, in all directions. The number of packets applied per snapshot was fixed to obtain a well-converged, logarithmic mean velocity profile, where the magnitude of the fiber circulation was

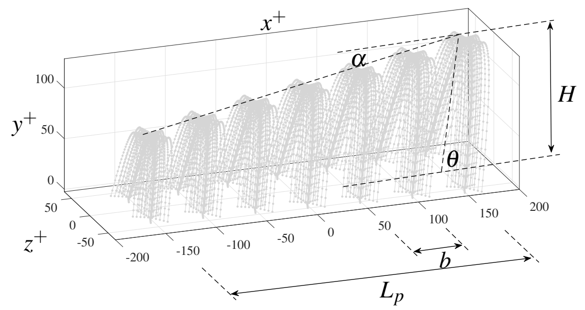

Figure 2: The smallest hairpin packet, $H \approx 128$, illustrating the discrete vortex fibers used to calculate the packet-induced velocity via Biot-Savart.

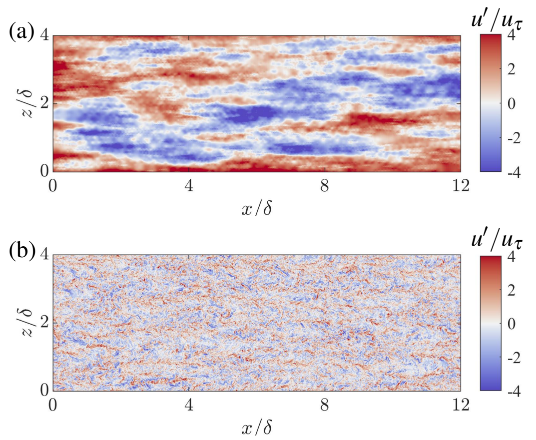

Figure 3: Wall-parallel maps of the fluctuating streamwise velocity, u', at $y^+ \approx 176$ for (a) the attached eddy simulation and $y^+ \approx 281$ (b) the channel DNS. $y^+ = 3.9\sqrt{Re_\tau}$ corresponds to the middle of the log layer for both cases.

used as an arbitrary fitting parameter to obtain the desired von Karman slope ($1/\kappa$), where all packets were assumed to advect at the free-stream velocity.

An example of the resulting instantaneous, wall-parallel velocity field is shown in figure 3(a), with comparison to the corresponding field obtained from a channel flow DNS at $\mathrm{Re}_\tau = 5200$ by Lee & Moser (2015), shown in figure 3(b). The simulated field exhibits meandering, low- and high-speed velocity regions characteristic of experimentally observed flows, but clearly composed of much larger, more coherent scales, similar to a low-pass filtering of the DNS field.

The streamwise energy spectra for the simulated velocity field were calculated by averaging over $N = 480$ snapshots until statistical convergence was obtained. A map of the premultiplied energy spectra is shown in figure 4 for (a) the attached eddy simulation and (b) the corresponding DNS. We note first that the simulated velocity field is limited by the spatial resolution near the wall and thus begins at $y^+ = 20$. However, the attached eddy model is designed to primarily represent the coherent structures inhabiting the log-layer, and thus this limitation is not significant. Secondly, we observe that the DNS spectral map shows the expected two regions of intense spectral energy, associated with the small scale motions involved in the near wall cycle at $y^+ \approx 15$, and LSMs inhabiting the outer-peak, at the center of the log layer. The attached eddy simulation captures only this second spectral signature of LSMs in the center of the log layer.

Moreover, the spectral energy in the attached eddy simulation has a peak around $k \approx 1$ and is thus associated with a region of wavenumbers lower than those corresponding to the packet sizes themselves ($k \approx 3$–43), indicating the streamwise alignment of individual packets to generate large-scale, meandering motions. The early implementations of the numerical attached eddy simulation by Perry (1987) also found a significant energy shift to lower wavenumbers, in comparison to experiments, although they found a peak energy around $k \approx 8$. The precise shape of the energy spectrum for the attached eddy simulation is largely determined by the shape of the eddy itself, as noted by Marusic & Perry (1995); in the present study we examined only a parabolic, λ-shaped hairpin.

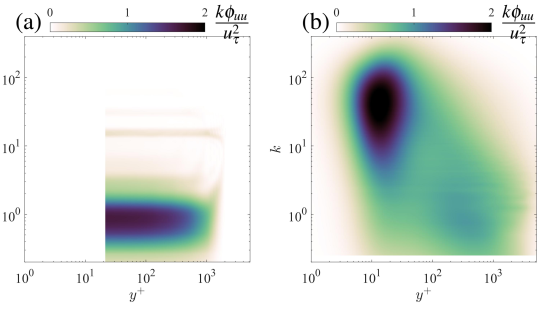

Figure 4: Pre-multiplied, streamwise energy spectra for (a) the attached eddy simulation and (b) the channel DNS. The wavenumber, k, is normalized by the channel half height.

RESULTS

Bicoherence of the Attached Eddy Model

Having verified the spectral energetic structure of the attached eddy model, the streamwise bispectrum was calculated according to (1) and then normalized by the energy spectral density associated with the different wavenumber triads to obtain the bicoherence, $b(k', k'')$. Because the attached eddy model is composed of mostly LSMs, a significant amount of its spectral energy resides at wavenumbers near the wavenumber of the finite computational domain. This can result in significant spectral leakage, which becomes particularly prominent in the bispectral calculation, and thus special care was taken with the removal of the DC component of the velocity signals, as described in the Appendix. The bicoherence map evaluated at the middle of the log layer is shown in figure 5.

The bicoherence map for the attached eddy simulation differs significantly from that of the channel flow DNS at the same wall-normal location, shown above in figure 1(a). In the channel flow, the bicoherence indicated a continuous band of strong coupling between the LSMs and the full range of other scales in the flow, which was interpreted in the context of large-scale modulation of the small scales. For the attached eddy simulation, the bicoherence indicates a discrete set of strong triadic couplings between scales that differ in wavenumber by an order of magnitude, such that $k'' \approx 10k'$. The fact that the most prominent bicoherence is constrained along this line indicates that large-scales interact most strongly with scales that are substantially smaller, by an order of magnitude, and not with scales at neighboring wavenumbers. Perhaps this is partly explained by the relative lack of small-scale structures in the attached eddy construction.

The bicoherence across the $k'' \approx 10k'$ slice is shown in figure 6, along with circle-symbols for wavenumbers corresponding to the streamwise extent (L_p) for the different discrete packets. The three largest packets are associated with

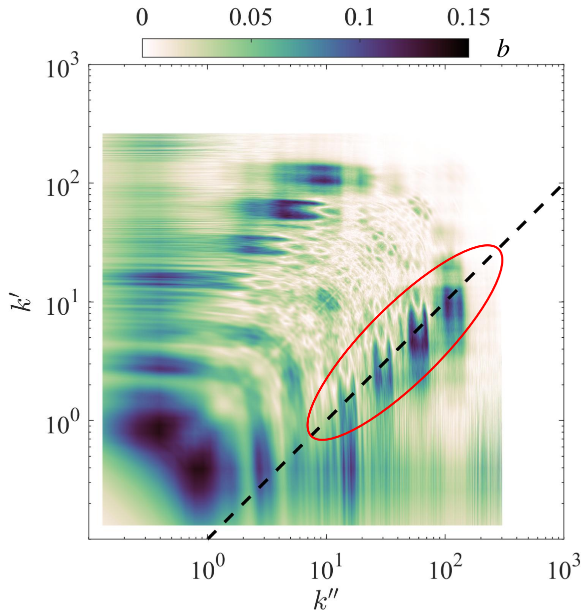

Figure 5: Bicoherence map in the middle of log layer ($y^+ = 3.9Re_\tau^{1/2} \approx 176$) for the attached eddy simulation at $Re_\tau = 2048$. The red ellipse marks the region of high bicoherence associated with the wavenumber triad defined by k' and $k'' \approx 10k'$, denoted by the black dashed line.

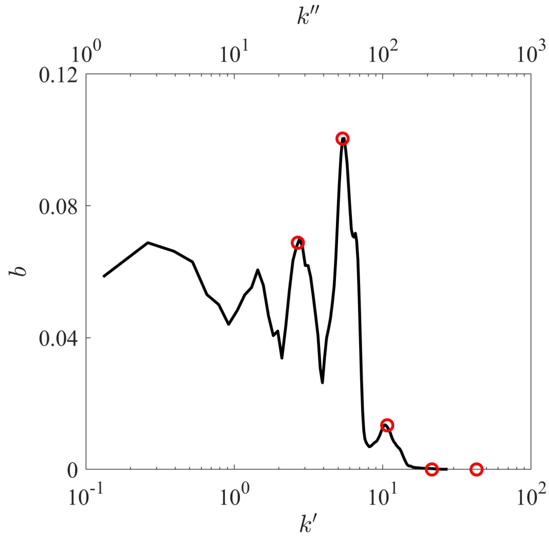

Figure 6: The bicoherence slice along $k'' = 10k'$ in the middle of the log layer taken from figure 5 is shown in the black line. The sharp peaks appear at wavenumbers in multiples of 2. The wavenumbers corresponding to the streamwise extent (L_p) of the individual hairpin packets, $k' = \{2.7, 5.4, 10.7, 21.4, 42.9\}$, are marked with red circles. The lowest-wavenumber, sharp peak in the bicoherence corresponds to $k' = 1.4$, which is twice the size of the largest hairpin packet. The broader peak in bicoherence at the lowest wavenumbers is the result of spectral leakage as discussed in the Appendix.

prominent peaks in bicoherence, whereas the smaller packets are not. There is also a sharp bicoherence peak at twice the size of the largest packet. The question about the interpretation of this high bicoherence region thus remains: why the largest packets don't seem to interact with the next largest packets in the packet hierarchy, i.e. why packets separated by a single generation don't show significant bicoherence and exhibit a high bicoherence along $k'' \approx 2k'$?

The precise peak locations in the bispectrum likely reflect the spatial location of the packets in the flow; modifying the placement of the packets from the entirely random process used here to a constrained random process that controls the minimum distance between similar packets, as discussed in de Silva *et al.* (2016), is expected to alter the observed peak structure of the bicoherence. Thus, the lack of observed interactions between neighboring packets may be attributed to their relative spatial orientation in the flow and perhaps due to a lack of overlap, although this question remains unresolved. The convection velocity of the individual packets is also expected to influence the interaction behavior captured by the bicoherence.

Finally, it is worth noting that the bicoherence is constructed to represent the triadic coupling between scales, which results from a non-linear interaction. In the attached eddy model, however, the non-linear interaction is simulated via a purely linear superposition of scales, and nevertheless the bicoherence detects the scale-interactions as if they were due to non-linear coupling. This provides direct evidence that the linear superposition process used in attached-eddy type models can be shown to emulate even the non-linear coupling associated with the turbulent convection.

Biphase of the Attached Eddy Model

The biphase can be interpreted as a measure of the interaction delay between two velocity modes interacting to transfer energy to a third. Indeed, we showed previously that the averaged biphase is directly related to the direction of the turbulent energy cascade. In the case of the DNS channel flow, shown above in 1(b), the biphase was shown to vary with wavenumber, where nearly all triads exhibited positive interaction delays ($\beta > 0$, i.e. all shades of red in the bipshase map), consistent with the classical energy cascade. However, as noted in the introduction, the precise interpretation of the interaction delays was unclear: were they associated with the geometry and spatial distance between the interacting modes or a temporal delay in the interaction dynamics? The attached eddy model removes the non-linear dynamics because the velocity field is constructed entirely by means of linear superposition of hairpin packets. Therefore, for the attached eddy biphase calculation, the delay interpretation is more naturally associated with spatial distance between scales and the physical geometry of the interacting modes. The biphase map evaluated at the middle of the log layer is shown in figure 7.

Unlike the DNS biphase which was almost uniformly positive, the attached eddy biphase exhibits both positive and negative delays, depending on the wavenumber triad. Following along the $k'' = 10k'$ slice of significant bicoherence, we see that the biphase is positive, as in the DNS. But, if instead, we followed along the $k' = 1$ line of the LSM interactions, then there is a transition between positive and negative biphase. Large-scale interactions with neighboring large scales show a positive delay, but large-scale interactions with small-scales show a negative delay. This suggests that if the high bicoherence region could be shifted or extended by means of modification of the superposition algorithm, then the biphase may also follow suite, and thus the interaction delay can be tuned by the spatial orientation and placement of the packets.

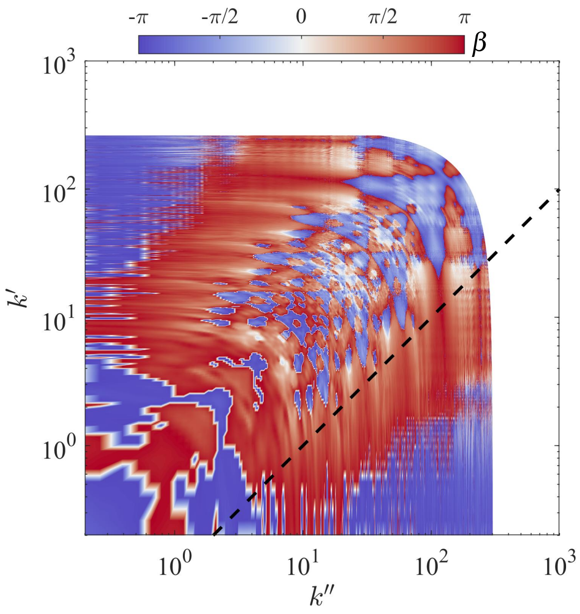

Figure 7: The streamwise biphase map in the middle of log layer ($y^+ = 176$). The black dashed line is the same line as in figure 5.

CONCLUSIONS

Bispectral calculations were performed for a modest Reynolds number attached eddy simulation, with five generations of hairpin packets, and contrasted with a DNS channel flow. The bicoherence showed evidence for non-linear coupling between large- and small-scale motions, even though the simulation itself involved only linear superposition of hairpin packets, thus providing evidence that the spectral features of non-linear dynamics can be modeled using linear models alone. However, the nature of the scale-interactions for the attached eddy model was much narrower in wavenumber-space than that of the DNS, and indicated that only a limited set of wavenumber triads participated. The sliced bicoherence was used to identify the specific hairpin packets participating in these interactions. The biphase, which has been shown to represent an interaction delay between different wavenumber modes, and also the direction of average energy transfer due to the interactions, was shown to exhibit the same sign for the attached eddy model as for the DNS, at least in the region of high bicoherence. Overall, these results suggest that modification of the linear superposition mechanism in the attached eddy model is the key to altering the bispectral signature of the scale-interactions, and thus the key to allowing the attached eddy model to more realistically capture true, non-linear dynamics in wall-bounded flows.

APPENDIX

The typical procedure for removing the DC component of a random signal, $z(t)$, as described by Bendat & Piersol (1986), prescribes subtracting the mean, $\langle z(t)\rangle$ from the instantaneous signal, and then tapering the resulting data with an appropriate window, after which the discrete Fourier transform (DFT) is calculated, with zero-padding. However, this procedure can introduce significant artifacts to the resulting energy spectrum (or bispectrum) when the original signal is dominated by very low frequency (wavenumber) components, in which case most of the signal may be offset from zero even if, arithmetically, it

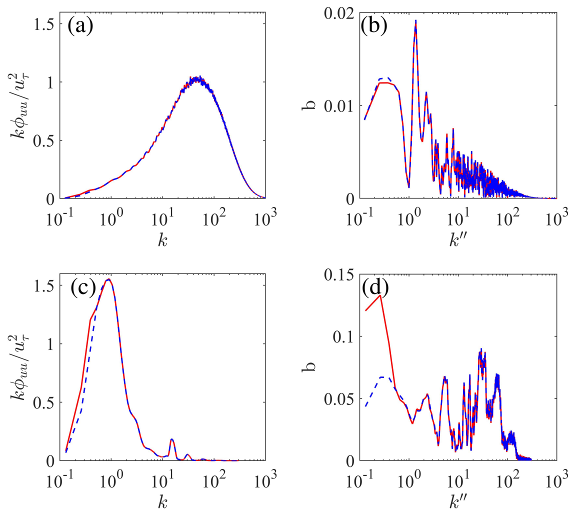

Figure 8: Premultiplied streamwise energy spectra (a,c) and bicoherence calculations (b,d) for the DNS (top) and attached eddy (bottom) where the red line indicates unweighted DC component removal and the blue line indicates the window-weighted DC component removal. Note the significant reduction in DC leakage for the attached eddy bicoherence (d) when using the window-weighted mean, in contrast to the minimal effect in all other calculations. The bicoherence in (b) and (d) is measured along $k' = 2$; all spectral measurements are at the middle of the log layer.

has zero mean. When this happens, the windowing process can actually introduce spurious energy at low frequencies. In order to avoid this spectral leakage from the DC and near-DC components, Van der Schaaf & Van Hateren (1996) suggest that a 'window-weighted' average be removed from the instantaneous signal instead of the traditional, unweighted averaged. The window-weighted average, $\langle z(t)\rangle_w$ for a given window function, $w(t)$, is defined as

$$\langle z(t)\rangle_w = \langle z(t)w(t)\rangle / \langle w(t)\rangle \tag{2}$$

Once this average is removed, then the resulting signal can be tapered and the DFT can be calculated following the standard procedure.

The difference between the standard DC removal and the weighted DC removal is shown in figure 8 for both the DNS data, with predominantly higher wavenumber components, and the attached eddy data, with predominantly lower wavenumber components. The greatest leakage without weighting is observed in the bicoherence for the attached eddy, and that is the case in which the weighting produces the most significant improvement. The choice of DC removal has little impact on the other calculations.

REFERENCES

Bandyopadhyay, P. R. & Hussain, A. K. M. F. 1984 The coupling between scales in shear flows. *Physics of Fluids* **27** (9), 2221–2228.

Bendat, J.S. & Piersol, A.G. 1986 *Random Data: Analysis and Measurement Procedures*, 4th edn. Wiley.

Cui, G. & Jacobi, I. 2021 Biphase as a Diagnostic for Scale Interactions in Wall-Bounded Turbulence. *Physical Review Fluids* **6** (1), 014604.

Duvvuri, S. & McKeon, B. J. 2015 Triadic scale interactions in a turbulent boundary layer. *Journal of Fluid Mechanics* **767**, 1–11.

Eich, F., De Silva, C. M., Marusic, I. & Kähler, C. J. 2020 Towards an improved spatial representation of a boundary layer from the attached eddy model. *Physical Review Fluids* **5** (3), 1–13.

Lee, M. & Moser, R. D. 2015 Direct numerical simulation of turbulent channel flow up to $\mathrm{R}e_{\tau} \approx 5200$. *Journal of Fluid Mechanics* **774**, 395–415.

Marusic, I. & Perry, A. E. 1995 A wall-wake model for the turbulence structure of boundary layers. Part 2. Further experimental support. *Journal of Fluid Mechanics* **298**, 389–407.

Mathis, R., Hutchins, N. & Marusic, I. 2009 Large-scale amplitude modulation of the small-scale structures in turbulent boundary layers. *Journal of Fluid Mechanics* **628**, 311–337.

Perry, A. E. 1987 Turbulence Modelling Using Coherent Structures in in Wakes , Plane Mixing Layers and Wall Turbulence. In *Perspectives in Turbulence Studies* (ed. H. U. Meier). Springer-Verlag Berlin.

Perry, A. E. & Chong, M. S. 1982 On the mechanism of wall turbulence. *Journal of Fluid Mechanics* **119**, 173–217.

Schmidt, O. T. 2020 Bispectral mode decomposition of nonlinear flows. *Nonlinear Dynamics* **102**, 2479–2501.

de Silva, C. M., Woodcock, J. D., Hutchins, N. & Marusic, I. 2016 Influence of spatial exclusion on the statistical behavior of attached eddies. *Physical Review Fluids* **1** (2).

Van der Schaaf, A. & Van Hateren, J. H. 1996 Modelling the power spectra of natural images: Statistics and information. *Vision Research* **36** (17), 2759–2770.